Journal of CO2 Utilization 77 (2023) 102614

Contents lists available at ScienceDirect

Journal of CO2 Utilization

journal homepage: www.elsevier.com/locate/jcou

Nickel supported on polymeric graphitic carbon nitride for electrocatalytic in reduction of carbon dioxide

Walker Vinícius Ferreira do Carmo Batista [a], Jessica Fernanda Coelho [b], Wanessa Lima de Oliveira [a], Nivaldo Gomes Pereira Filho [b], Eduarda Ferreira de Oliveira [a], Taís dos Santos da Cruz [a], Hidila Souza Teixeira da Silva [c], Gleison Neres Marques [d], João P. de Mesquita [a,d], Rodrigo F.B. de Souza [b], Almir O. Neto [b,*]

[a] Department of Chemistry – Federal University of Jequitinhonha and Mucuri Valleys, Rodovia MGT 367 - Km 583, n° 5000, Alto da Jacuba, Diamanntina, MG CEP 39100-000, Brazil
[b] Instituto de Pesquisas Energéticas e Nucleares, IPEN-CNEN/SP, Cidade Universitária, Av. Prof. Lineu Prestes, 2242, São Paulo 05508-900, SP, Brazil
[c] School of Chemical Engineering, Federal University of Uberlândia, Uberlândia, MG 38408-144, Brazil
[d] Department of Chemistry – Federal University of São Carlos, Rod. Washington Luís km 235 - SP-310, São Carlos, SP CEP 13565-905, Brazil

ARTICLE INFO

Keywords:
CO_2RR
CN-Ni doped
CO_2 to Methanol

ABSTRACT

This study explores the potential of carbon-based materials, specifically CN-Ni-doped, as catalysts for CO_2 reduction to methanol in a PEM-R. The research investigates the impact of Ni incorporation on CN's structure, resulting in increased interlayer spacing and reduced crystallite size. Additionally, the introduction of Ni modifies the samples' morphology, creating a more compact structure with smaller sheets. The findings indicate that CN-Ni displays promising catalytic activity, achieving a 25% Faradaic Efficiency (FE) with a methanol production rate of approximately 1.1 mol L^{-1} h^{-1}. The study underscores the significance of optimizing reactor operational parameters to enhance CO_2RR. In conclusion, this research contributes to the advancement of efficient and sustainable approaches for CO_2 utilization and methanol synthesis.

1. Introduction

Reducing CO_2 emissions represents one of the greatest challenges in slowing down climate change. However, this task is extremely challenging because carbon dioxide production is associated with many economic activities, making it difficult to reduce emissions without causing harm to the economy. Therefore, it is important to develop new technologies, and electrochemistry is one promising route to reducing CO_2 emissions and remediation [1]. The process involves reducing CO_2 in an electrochemical cell, converting it into more useful compounds, such as methanol, formic acid, and formaldehyde [2,3].

The CO_2 reduction reaction (CO_2RR) to obtain products is not a trivial task due to the linear molecule of carbon dioxide with two equivalent C = O bonds, with an energy is equal to 750 kJ mol^{-1}, which is twice the binding energy of other carbon-based compounds on average [4]. The main proposed reaction paths follow simplified steps:

$$CO_{2(g)} \rightarrow CO_{2(ads)} \quad (1)$$

$$CO_{2(ads)} + H^+ \leftrightarrow HCOO^+ \quad (2)$$

$$HCOO^+ + H^+ \leftrightarrow HCOOH \quad (3)$$

$$HCOOH + H_2 \leftrightarrow H_2CO + H_2O \quad (4)$$

$$H_2CO + H_2 \leftrightarrow H_3COH \quad (5)$$

Thermodynamically discussing, the initial step in reducing CO_2 (represented by Eq. 2) requires an overpotential of − 1.9 V under standard conditions. It is noteworthy that this overpotential is considerably higher compared to that required for the hydrogen evolution during the water breaking process [5]. In addition to the loss of faradaic efficiency due to the competition of H_2 evolution, the electrolyte decomposition shifts the potentials between the electrodes, which can alter the reaction paths [6]. Since the primary challenge is to reduce this overpotential, studies of composition, morphology, preferential phase, and adding functional groups to the material are being conducted [7–12].

* Corresponding author.
E-mail address: aolivei@usp.br (A.O. Neto).

https://doi.org/10.1016/j.jcou.2023.102614
Received 24 July 2023; Received in revised form 2 October 2023; Accepted 22 October 2023
Available online 7 November 2023

In this context, two interrelated strategies are being utilized. The first strategy involves the development of catalyst materials for the reaction, and among the materials under investigation are carbon-based materials that have demonstrated the ability to inhibit particle agglomeration on their surface, chemical stability and thermal, conductivity wide versatility for textural structural modification and functionalization with different functional groups [13–15].

Among these carbon-based materials is CN, which contains a backbone of C-N bonds and a high concentration of N sites situated at specific locations on the s-triazine or s-heptazine units. Additionally, CN possesses a high concentration of N-H functional groups that provide Brønsted acid sites and Lewis base sites, along with an abundance of binding sites for metals. Furthermore, the π-π conjugation binding structure of these materials is highly favorable for metal deposition [16, 17].

CN is a semiconductor renowned for its distinctive structure, and it finds extensive application in photocatalysis and electrocatalysis owing to its remarkable synergistic effects when combined with metals and metal oxides [18]. In particular, carbon nitride decorated with nanoparticles exhibits outstanding catalytic activity, primarily attributed to the functional groups present in CN that promote CO_2 adsorption and facilitate charge transfer between the supporting material and the active center. Additionally, the high dispersion of nanoparticles within the support further enhances the catalyst's performance. The introduction of a metal catalyst assists in shifting oxygen, thereby facilitating the hydrogenation process [19]. In this case the addition of CN-metal doped present advantages, including chemical stability, absorbency, and modifiable structural and electrical properties [20]. The incorporation of Ni nanoparticles adds to their low cost and high activity for various processes, including reforming, decomposition, partial oxidation, and hydrogenation [21–23].

On the other hand, various reactor designs have been developed to optimize CO_2 reduction reaction (CO_2RR). Ju et al.[24] suggest that aspects of CO_2RR can be optimized not only through the use of specific materials but also by adjusting reactor operating parameters, such as electrolytes, temperature, CO_2 delivery pressure, electrode distances, and even reactor architecture [25–29]. Recently, Gutierrez-Guerra et al. [30] successfully reduced CO_2 using a proton exchange membrane reactor (PEM-R) similar to a fuel cell, for this reaction [28,30,31]. In this context, the present study focuses on investigating CO_2RR on CN-Ni doped material for methanol production in a PEM-R.

2. Experimental

The CN materials used in this study were synthesized by mixing 5 g of melamine in 100 mL of hot distilled water. The pH was adjusted between 3 and 4 and the mixture was stirred magnetically for 4 h. After cooling, the solution was filtered and dried for 24 h at 65 °C. The resulting solid was pyrolyzed in a crucible for 2 h in a muffle at 550 °C with a heating rate of 5 °C min^{-1} under nitrogen flow. For the synthesis of the CN-Ni, 4.75 g of melamine and 1.24 g of $Ni(NO_3)_2.6\ H_2O$ were used following experimental protocols as in CN-p sample preparation.

The synthesized CN materials were characterized using X-ray diffraction (XRD) and Fourier transform infrared (FTIR) spectroscopy. XRD analysis was performed using a Shimadzu XRD-6000 diffractometer with Cu Kα (λ = 1.54086 Å) as the source. The infrared spectra were acquired using KBr pellets in a Thermo Scientific Nicolet 6700 spectrometer.

The elemental composition (CHNS) was obtained with a LECO@CHNS/O analyzer, model TruSpec Micro. Thermogravimetric analysis (TGA) was conducted using a LABSYS EVO STA simultaneous TGA/Differential thermal analysis analyzer at a heating rate of 10 °C min^{-1} under constant oxygen flow (50 mL min^{-1}). The surface charge properties of the CN were determined from their zeta potential values in aqueous suspension (0.5 mg/mL), and zeta potential was measured on a Malvern Zetasizer Nano instrument (Malvern Instruments, USA). Scanning electron microscopy (SEM) images of the samples were obtained using a HITACHI model TM-3000 (Japan) equipment. The samples were fixed on a sample holder (stub) using a double-sided conductive carbon tape (TED PELLA brand), and the set was coated with gold in a plasma metallizer (Sputter Q150R ES from Quorum Technologies). The textural characterization of the CN materials was carried out using the N_2 adsorption–desorption isotherms method with a Micromertics ASAP 2020 apparatus (Shanghai, China).

The amount of nickel anchored in the CN samples was determined from atomic absorption spectroscopy using a Varian spectrometer, model AA 50B. Approximately 0.34 mg of sample was accurately weighed and added into a round bottom flask containing 5 mL of concentrated H_2SO_4, 5 mL of concentrated nitric acid, and 5 mL of H_2O_2 (30%). The mixture was refluxed for 7 h and then filtered. The solution was then diluted to 25 mL. The analytical curve used for quantification of nickel (II) was prepared with 11 standards in the concentration range from 0 to 16 ppm. The calibration curve had a linear equation of y = 0,0061[nickel] - 0,0006 with an r^2 value of 0.9998.

The catalysts were further characterized by cyclic voltammetry performed in a three-electrode electrochemical cell using a PGStat 302 N Autolab potentiostat, with a working electrode built on a glassy carbon (0.2 cm^2) support covered with an ultra-thin porous layer produced from a paint made with 5 mg of CN materials and 5 mg of carbon Vulcan, 1800 μL of ultrapure water, 1200 μL of isopropanol, and 50 μL of Nafion® (D-520) mixed using ultrasound. An Ag/AgCl 3.0 mol L^{-1} electrode was used as a reference electrode, and a 2 cm^2 Pt electrode was used as a counter electrode. The same potentiostat and electrodes were used in conjunction with a Raman Macroram spectrometer—Horiba, with a 785 nm laser, and an electrochemical cell suitable for carrying out the electrochemical assays assisted by in-situ Raman spectroscopy, as reported by De Souza [32].

The conversion of CO_2 to methanol was carried out in a PEM-R, with electrodes constructed with 1 mg cm^{-2} of CN materials with vulcan carbon (20% w/w) at the cathode, a membrane of Nafion 117 as electrolyte, and 1 mg cm^{-2} of Pt/C Basf (20% w/w) as the anode. All electrodes were prepared by depositing the ink containing the catalyst with 30% by mass of a solution of Nafion® D-520 (Aldrich) and isopropanol applied by brushing on a carbon cloth treated with PTFE. The reactor is based on a typical fuel cell coil plate design made of 316 L steel, fed with 10 mL min^{-1} of CO_2 at cathode and 300 mL min^{-1} of humidified H_2 at 85 °C on the anode. After the reaction, aliquots of the reactor effluent were collected and analyzed using infrared spectroscopy and high-performance liquid chromatography (HPLC) with a UV/Vis detector. The HPLC analysis was performed using a flow rate of 0.8 mL min^{-1} of a solution of 50% water, 40% acetonitrile, and 10% sodium acetate buffer on a C18 column (Phenomenex Luna 5 μm, 250 × 4.6 mm). The calibration curve had a linear equation of peak area = 59.916 + 238.59 [methanol] with an r2 value of 0.9981.

3. Results and discussion

The X-ray diffraction patterns of CN-p, CN-Ni, and NiO are presented in Fig. 1. Two distinct diffraction peaks are evident at 2θ values of 13.03° and 27.73°, respectively. The first peak is generated as a result of the ordered plane of tris-s-triazine units, designated as the (100) plane, while the second peak is assigned to conjugated aromatic stacking and indexed as the (002) plane [33].

Additionally, there are peaks at approximately 37° and 43° at 2θ values, corresponding to the crystallographic planes (111) and (200) of NiO (COD 96–432–9324). The interlayer d-spacing values for CN-p and CN-Ni were found to be 0.82 Å and 0.87 Å, respectively. Furthermore, a slight displacement of the (002) plane was observed, indicating that the insertion of Ni increased the distance between the layers due to the metal's large ionic radius. It is worth noting that Deraman and coworkers [34] have suggested that an increase in interlayer d-spacing for 2D materials such as graphene leads to a reduction in the average

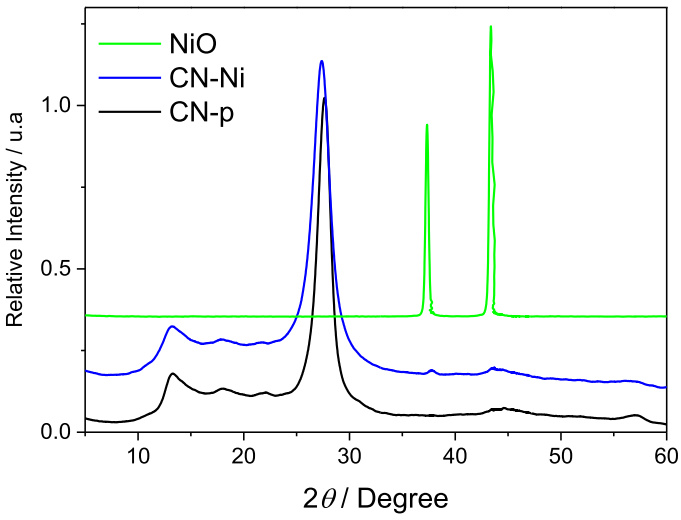

Fig. 1. XRD pattern of CN-p, CN-Ni and NiO.

crystallite size, which is analogous to the observations made for the CN materials investigated in this study.

The FTIR spectra, as shown in Fig. 2, reveal several bands associated with specific chemical groups present in the samples. A sharp band, observed at 810 cm^{-1}, corresponds to the breathing mode of triazine units in CN-p [35]. The bands at 1570 and 1640 cm^{-1} are attributed to the bending of single bond N-H and stretching of C═N double bond bonds, respectively. The bands between 1241 and 1480 cm^{-1} are assigned to the stretching vibrations of the single bond C-N [35]. The presence of nickel is evident from the bands observed at approximately 600 and 492 cm^{-1}, corresponding to Ni-O [36,37] and Ni-N nanostructures [37,38], respectively.

Fig. 3a illustrates the evolution of mass loss and heat flow with temperature for CN-Ni. The DTA analysis reveals the presence of three primary stages of decomposition, as depicted in Fig. 3b. The data show an initial endothermic peak with a maximum at 58 °C, leading to a mass loss of approximately 1.4% of the total weight, which can be attributed to the removal of surface water. The second step is observed between 110 °C, with a mass loss ranging from 1.0% to 2.9%, likely associated with the elimination of structural water. The process of carbon-nitrogen loss for the composites occurs at temperatures around 500 °C, with the maximum degradation process of the carbon nitride structure observed at 715 °C for CN-p and 615 °C for CN-Ni [39]. The incorporation of nickel into the graphitic carbon nitride structure results in decreased stability due to metal catalysis, leading to a greater mass residue formation attributed to the presence of NiO_2 [40].

The Zeta potential measurements for CN-p (−31.8 mV) are consistent with the literature [41]. However, for the CN-Ni material (−35.8 mV), the Zeta potential shifts towards more negative values, primarily due to the presence of oxidized species of the incorporated metal within the structure [42]. As shown in Table 1, the proportion of carbon and nitrogen decreases, while hydrogen remains unchanged. The percentage of nickel in the sample prepared with 5% nickel, CN-Ni, was determined to be 4.76% through Atomic Absorption Spectrometry.

The optical characteristics of CN-p and CN-Ni samples were examined through UV-Vis diffuse reflectance spectroscopy (DRS), revealing variations and changes in the electronic structure of CN-p upon the addition of nickel. This is prominently highlighted in the UV-Vis spectroscopy results (Fig. 1$ (A)), where distinct shifts are observed. These shifts indicate that the presence of Ni significantly influences the electronic structure of CN-p, resulting in alterations to its optical and electronic properties [43]. The band gaps were estimated from graphs of the square root of the Kubelka-Munk functions plotted against photon energy (Fig. 1$ (B)). The band gaps for CN-p and CN-Ni were found to be 2.82 and 2.98 eV, respectively. These findings clearly demonstrate that the introduction of nickel brings about changes in the electronic properties of graphitic carbon nitride, which could have a direct correlation with its catalytic properties for the reduction of CO_2 to methanol.

The investigation of the local morphologies of the synthesized materials through SEM analysis, as illustrated in Fig. 4, yielded significant insights. In the low-magnification SEM image, it becomes apparent that both CN-p and CN-Ni are predominantly composed of large, irregular-shaped particles with dimensions in the micron range. This aligns with the characteristic appearance of bulk materials, where strong van der Waals interactions between layers give rise to a slate-like, stacked lamellar structure [16]. However, the introduction of nickel into the CN-Ni composite led to a notable alteration in these morphological characteristics. This transformation can be attributed to the fragmentation of the polymeric carbon nitride structures, as supported by the XRD data. CN-Ni exhibits a more compact structure with smaller sheets, indicating that the bulk g-C3N4 may have undergone oxidation and exfoliation due to the presence of trace amounts of nickel during the melamine pyrolysis process.

To gain a deeper understanding of the elemental distribution within the compound's structure, Energy Dispersive Spectroscopy (EDS)

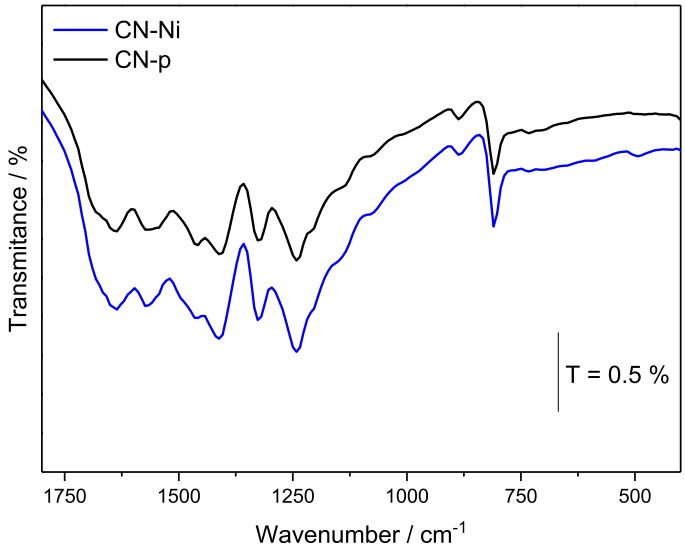

Fig. 2. Fourier-transform infrared spectroscopy characterization of modified carbon nitride with different nickel contents.

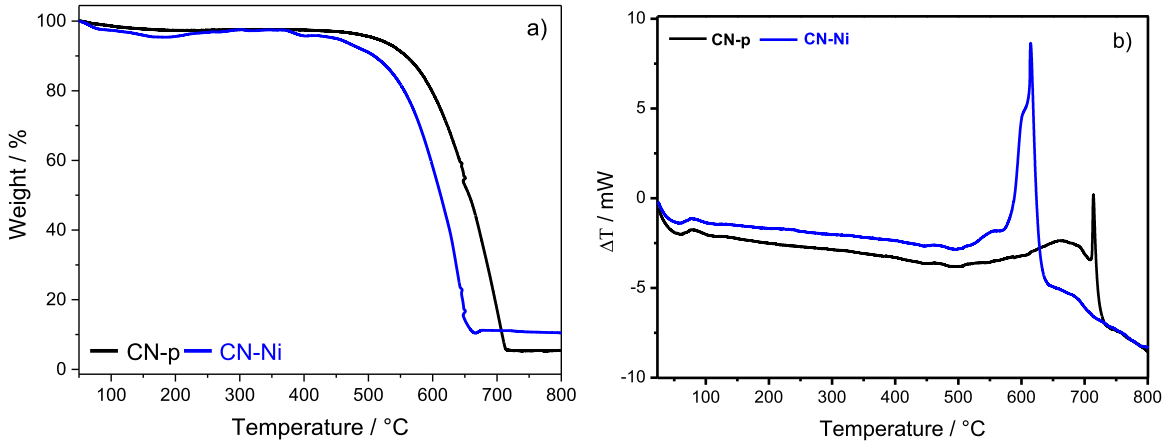

Fig. 3. a) Thermogravimetric analysis a) and differential thermal analysis;b) of the samples.

Table 1
Elementary composition of materials.

Sample	N[a] / %	C[a] / %	H[a] / %	Ni^{2+b} / %
CN-p	60.482	34.997	2.427	-
CN-Ni	58.366	33.361	2.398	4.76

[a] CHN elemental analysis
[b] Experimental values for Atomic Absorption Spectrometry.

analyses were conducted, as shown in Figs. 2 and 3. These analyses provided valuable insights into the spatial distribution of elements within the material. Particularly noteworthy is the nickel ion concentration, as determined through EDS element dot analysis and element mapping, which unveiled a uniform dispersion of nickel throughout the CN structure. The nickel content was quantified at approximately 5.05 wt%. The homogeneous distribution of nickel within the composite is a significant finding, suggesting that the incorporation of nickel into the CN-Ni material was well-controlled and consistent. This has important implications for the material's catalytic properties and its performance in various applications.

The nitrogen adsorption-desorption isotherms presented in Fig. 5 indicate that both CN-Ni and CN-p exhibit type IV isotherms with H3-type hysteresis, which is characteristic of mesoporous materials with slit-shaped pores. The pore distribution calculated by the Barrett-Joyner-Halenda (BJH) method during the desorption process confirms the presence of a mesoporous and macroporous architecture in both materials [44,45]. However, the introduction of Ni into CN results in a significant increase in the specific surface area, from 14.1 m2/g for CN-p to 29.33 m2/g for CN-Ni. This is more than a two-fold increase, and it suggests that Ni is promoting the formation of new pores and/or

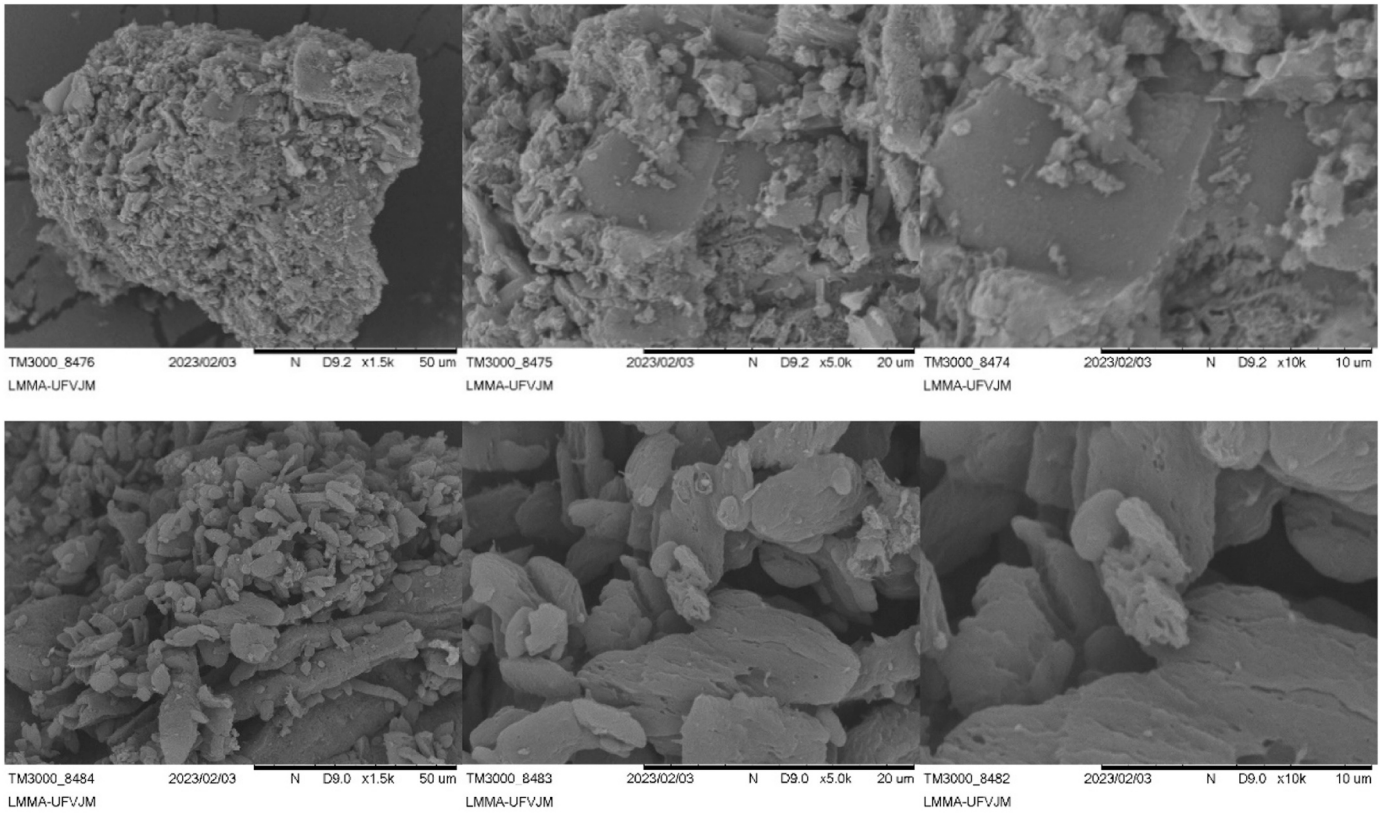

Fig. 4. SEM images of CN-p, CN-Ni.

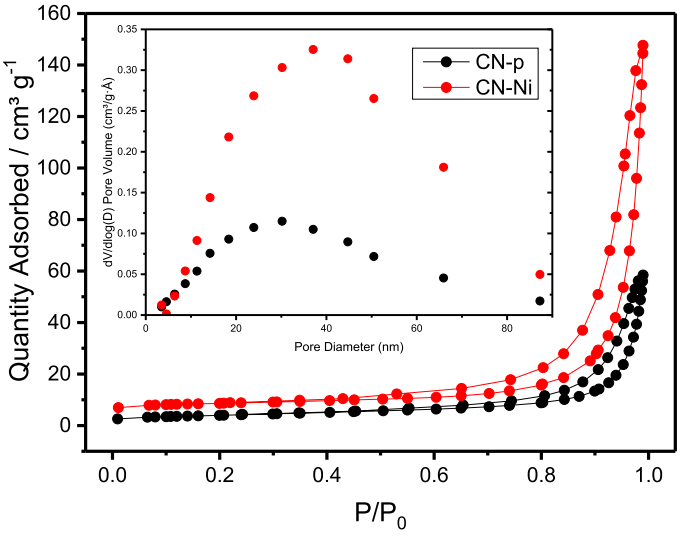

Fig. 5. N_2 adsorption-desorption isotherms of samples CN and the corresponding pore-size distribution curves (inset).

increasing the size of existing pores in CN. In addition to the increased surface area, CN-Ni also has a larger pore size (25 nm) than CN-p (20.9 nm). This is likely due to the fact that Ni is a larger atom than C and N, and it is therefore occupying more space within the pore structure. The larger pore size in CN-Ni also contributes to its higher pore volume (0.21 cm^3/g) compared to CN-p (0.09 cm^3/g). Indicating that the addiction os Ni into CN can be act as a template for pores, increasing the pore size in comparison with only CN, as a reported for others metals [46].

The CV curves presented in Fig. 6 for both materials exhibit quasi-rectangular shapes, suggesting favorable behavior for double electric layer capacitance. In the CV curve for CN-p, a reduction peak at − 0.15 V is observed, consistent with reports on CN-based materials [47]. However, the inclusion of nickel results in a reduction peak with reduced intensity and a shift towards less negative potentials. This shift is also observed in the voltammogram of a similar material doped with silver instead of nickel [48].

Fig. 7 shows the polarization curves of CN materials used in CO_2 reduction in PER-R, recorded within the potential range of 0.5 V to − 0.75 V. From the observed current density, it can be noted that CN-p performed inferiorly to CN-Ni. It is worth mentioning that the Ni-containing material displayed a more resolved linear voltammogram, where a reduction peak at − 0.1 V, seen at the same potential in Fig. 6 and inherent to the material, was followed by a reduction process at more negative potentials initiated at − 0.3 V, as reported by Lima [30].

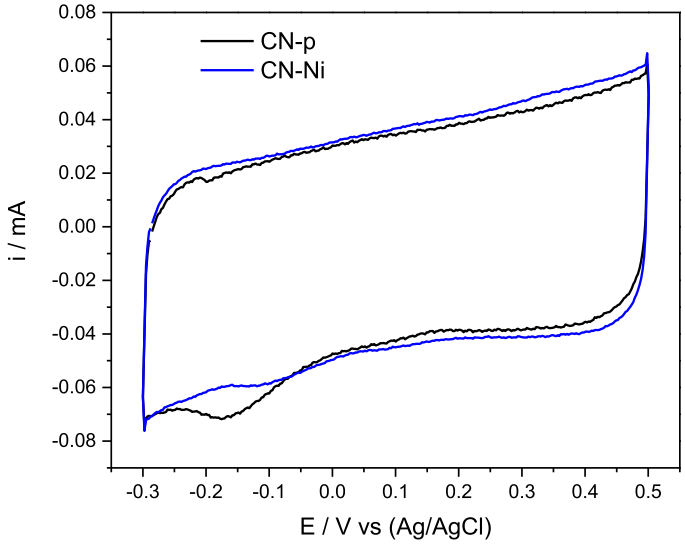

Fig. 6. Cyclic voltammetry of CN materials in $H_2SO_4$0,1 mol/L^{-1} (v = 10 mV/s).

The effluent collected from the CO_2RR process in the PER-FC reactor was subjected to FTIR spectroscopic analysis to characterize the products obtained. As shown in Fig. 8, the spectra of the effluent revealed the presence of a band at 1249 cm^{-1}, corresponding to the CH_2 rock formaldehyde vibration [49], that was observed at all tested potentials. However, when observing the CN-Ni system at different potentials, the band was only present at 0 and − 0.25 V. At more negative potentials, it was observed that two bands with appreciable intensities (~ 1080 cm^{-1} and 1030 cm^{-1}) appeared specifically for CN-Ni, which were concluded to be attributed to the methanol [50,51], as these bands were not observed for CN-p spectra.

CO_2RR has two significant factors to consider apart from the potential for forming each product. These factors are the rate of the reaction (r) and faradaic efficiency (FE). To determine the reaction rate (r) for methanol production, the amount of methanol measured by HPLC is used to calculate Eq. 6.

$$r = \frac{methanol \quad amount}{volume \quad x \quad time} \tag{6}$$

The reaction rate (r) is crucial in determining the amount of CO_2 converted per unit time and faradaic efficiency. Faradaic efficiency (FE) is a factor that measures the amount of energy expended per unit of methanol produced and is calculated using Eq. 2.

$$FE = \frac{6x \quad F \quad x \quad V \quad x[methanol]}{I \quad x \quad t} \tag{2}$$

The faradaic constant (F), solution volume (V), methanol concentration at a specific time (t) ([methanol]), and current intensity (I) are used in calculating FE. Fig. 9 summarizes r and FE at different potentials of CN materials.

The results obtained from the measurements showed that the CN-p catalyst interrupted the reduction of CO_2 in the initial stages with a slight formation of formaldehyde, without proceeding towards the production of further reduced products such as methanol. On the other hand, the catalyst containing nickel redirected the reaction towards the selective production of methanol, with faradaic efficiencies ranging between 20% and 25% for − 0.5 and − 0.75 V potentials. Indicating that nickel is fundamental for the CN act in CO_2RR.

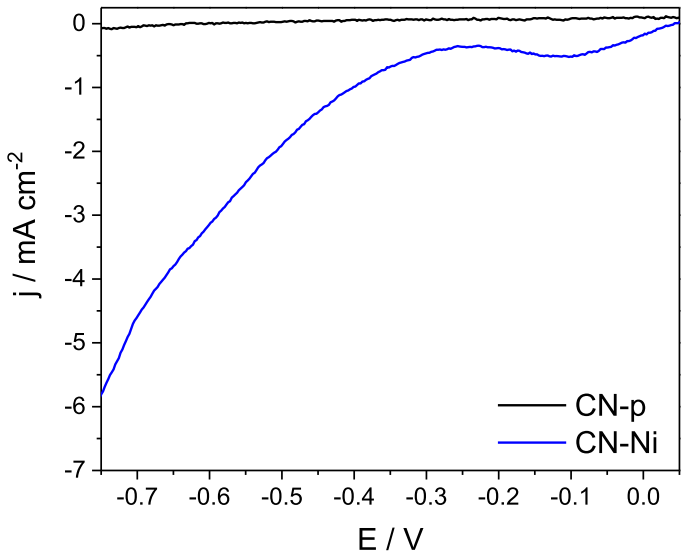

Fig. 7. j/V curves of CO_2RR in a PER-FC.

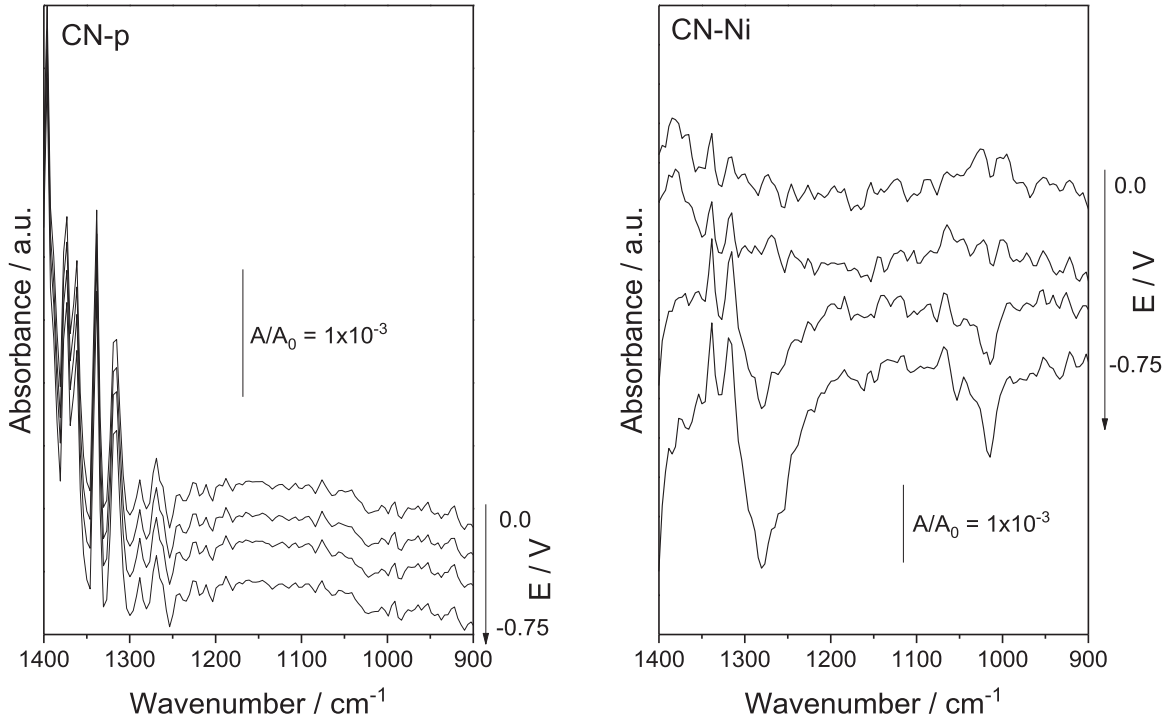

Fig. 8. Spectra of FTIR of PER-FC effluent collected in sodium acetate buffer collected at different potentials of the PEM-R output.

4. Conclusion

CO_2 reduction reaction on CN-Ni doped is promising to produce methanol. The study found that the insertion of Ni in the CN structure increased the distance between layers, leading to a reduction in the average crystallite size. The presence of nickel in CN was indicated by changes in FTIR spectra. DTA analysis indicated three stages of decomposition for CN-Ni, with the addition of nickel leading to a decrease in stability due to metal catalysis. The Zeta potential of CN-Ni shifted towards more negative values, mainly due to the presence of oxidized species of the incorporated metal in the structure. The addition of nickel caused changes in the morphology of the samples, leading to a more compact structure with smaller sheets. Both CN-p and CN-Ni exhibited type IV isotherms with H3-type hysteresis, indicating the presence of mesoporous and macroporous structures. These results highlight the potential of CN doped with Ni as a catalyst for the CO_2 reduction reaction to produce methanol with 25% of FE with r about 1.1 mol L^{-1} h^{-1}.

CRediT authorship contribution statement

Walker Vinícius Ferreira do Carmo Batista: Verification, replication/reproducibility of results/experiments. Jessica Fernanda Coelho: Verification, replication/reproducibility of results/experiments. Wanessa Lima de Oliveira: Verification, replication/reproducibility of results/experiments. Nivaldo Gomes Pereira Filho: Verification, replication/reproducibility of results/experiments. Eduarda Ferreira de Oliveira: Verification, replication/reproducibility of results/experiments. Taís

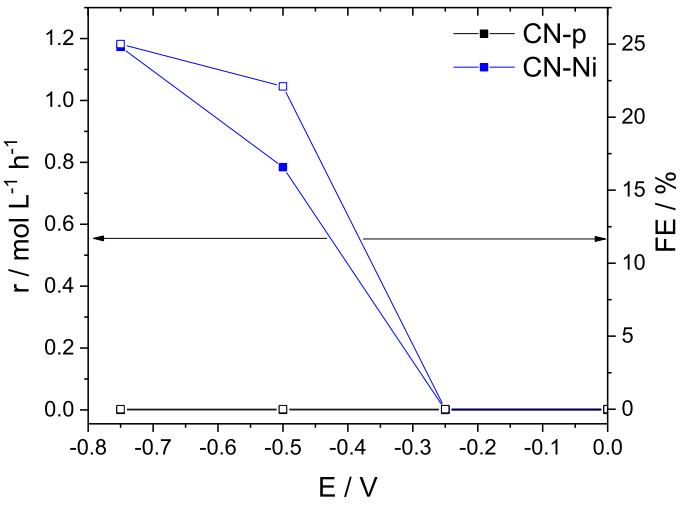

Fig. 9. Methanol efficiency production analysis by rate reaction (r) and Faradaic Efficiency (FE) driven under different potentials of CN-materials.

dos Santos da Cruz: Verification, replication/reproducibility of results/experiments. Hidila Souza Teixeira da Silva: Preparation, creation and/or presentation of the published work, specifically writing the initial draft. Gleison Neres Marques: Preparation, creation and/or presentation of the published work, specifically writing the initial draft. João P. de Mesquita: Preparation, creation and/or presentation of the published work by those from the original research group, specifically critical review, commentary or revision – including pre-or postpublication stages. Rodrigo F.B. de Souza: Management and coordination responsibility for the research activity planning and execution. Almir O. Neto: Acquisition of the financial support for the project leading to this publication.

Declaration of Competing Interest

The authors declare that they have no known competing financial interests or personal relationships that could have appeared to influence the work reported in this paper.

Data Availability

No data was used for the research described in the article.

Acknowledgment

The authors are grateful to CAPES, CNPq (302709/2020-7, 350514/2023-2), FAPESP (2017/11937-4) for financial support.

References

[1] U. Mondal, G.D. Yadav, Methanol economy and net zero emissions: critical analysis of catalytic processes, reactors and technologies, Green. Chem. 23 (2021) 8361–8405, https://doi.org/10.1039/D1GC02078A.
[2] D. Ješić, D. Lašič Jurković, A. Pohar, L. Suhadolnik, B. Likozar, Engineering photocatalytic and photoelectrocatalytic CO_2 reduction reactions: mechanisms, intrinsic kinetics, mass transfer resistances, reactors and multi-scale modelling simulations, Chem. Eng. J. (2020), 126799, https://doi.org/10.1016/j.cej.2020.126799.
[3] C. Kim, F. Dionigi, V. Beermann, X. Wang, T. Möller, P. Strasser, Alloy nanocatalysts for the electrochemical oxygen reduction (ORR) and the direct electrochemical carbon dioxide reduction reaction (CO2RR), Adv. Mater. 31 (2019), 1805617, https://doi.org/10.1002/adma.201805617.
[4] A.A. Khan, M. Tahir, Recent advancements in engineering approach towards design of photo-reactors for selective photocatalytic CO_2 reduction to renewable fuels, J. CO_2 Util. 29 (2019) 205–239, https://doi.org/10.1016/j.jcou.2018.12.008.
[5] H. Ooka, M.C. Figueiredo, M.T.M. Koper, Competition between hydrogen evolution and carbon dioxide reduction on copper electrodes in mildly acidic media, Langmuir 33 (2017) 9307–9313, https://doi.org/10.1021/acs.langmuir.7b00696.
[6] M. Ma, K. Djanashvili, W.A. Smith, Controllable hydrocarbon formation from the electrochemical reduction of CO_2 over Cu nanowire arrays, Angew. Chem. Int. Ed. 55 (2016) 6680–6684, https://doi.org/10.1002/anie.201601282.
[7] Z. Tao, Z. Wu, X. Yuan, Y. Wu, H. Wang, Copper–gold interactions enhancing formate production from electrochemical CO_2 reduction, ACS Catal. 9 (2019) 10894–10898, https://doi.org/10.1021/acscatal.9b03158.
[8] D. Yang, Q. Zhu, C. Chen, H. Liu, Z. Liu, Z. Zhao, X. Zhang, S. Liu, B. Han, Selective electroreduction of carbon dioxide to methanol on copper selenide nanocatalysts, Nat. Commun. 10 (2019), 677, https://doi.org/10.1038/s41467-019-08653-9.
[9] Y. Wang, H. Shen, K.J.T. Livi, D. Raciti, H. Zong, J. Gregg, M. Onadeko, Y. Wan, A. Watson, C. Wang, Copper nanocubes for CO_2 reduction in gas diffusion electrodes, Nano Lett. 19 (2019) 8461–8468, https://doi.org/10.1021/acs.nanolett.9b02748.
[10] K.J.P. Schouten, E. Pérez Gallent, M.T.M. Koper, Structure sensitivity of the electrochemical reduction of carbon monoxide on copper single crystals, ACS Catal. 3 (2013) 1292–1295, https://doi.org/10.1021/cs4002404.
[11] M.K. Kim, H.J. Kim, H. Lim, Y. Kwon, H.M. Jeong, Metal–organic framework-mediated strategy for enhanced methane production on copper nanoparticles in electrochemical CO_2 reduction, Electrochim. Acta 306 (2019) 28–34, https://doi.org/10.1016/j.electacta.2019.03.101.
[12] A. Glüer, S. Schneider, Iron catalyzed hydrogenation and electrochemical reduction of CO_2: the role of functional ligands, J. Organomet. Chem. 861 (2018) 159–173, https://doi.org/10.1016/j.jorganchem.2018.02.025.
[13] W. Yang, X. Shan, Y. Chen, Y. Gao, Enhanced photocatalytic performance of C3N4 via doping with π-deficient conjugated pyridine ring and BiOCl composite heterogeneous materials, Diam. Relat. Mater. 108 (2020), 107926, https://doi.org/10.1016/j.diamond.2020.107926.
[14] P. Zhao, J. Yan, B. Shan, Y. Zhang, Z. Zhao, L. Liu, Z. Su, W. Cheng, X. Xu, Copper nanoparticles control of carbon supported copper catalysts for dimethyl carbonate synthesis: A short review, Mol. Catal. 536 (2023), 112910, https://doi.org/10.1016/j.mcat.2022.112910.
[15] B. Pramanick, P. Felix Siril, Synergistic visible light plasmonic photocatalysis of bimetallic Gold-Palladium nanoparticles supported on graphene, Results Chem. 5 (2023), 100774, https://doi.org/10.1016/j.rechem.2023.100774.
[16] M. Ubaidullah, A.M. Al-Enizi, A. Nafady, S.F. Shaikh, K.Y. Kumar, M.K. Prashanth, L. Parashuram, B.-H. Jeon, M.S. Raghu, B. Pandit, Photocatalytic CO_2 reduction and pesticide degradation over g-C3N4/Ce2S3 heterojunction, J. Environ. Chem. Eng. 11 (2023), 109675, https://doi.org/10.1016/j.jece.2023.109675.
[17] N. Mansor, T.S. Miller, I. Dedigama, A.B. Jorge, J. Jia, V. Brázdová, C. Mattevi, C. Gibbs, D. Hodgson, P.R. Shearing, C.A. Howard, F. Corà, M. Shaffer, D.J.L. Brett, P.F. McMillan, Graphitic carbon nitride as a catalyst support in fuel cells and electrolyzers, Electrochim. Acta 222 (2016) 44–57, https://doi.org/10.1016/j.electacta.2016.11.008.
[18] S. Vignesh, S. Suganthi, M. Srinivasan, A. Tamilmani, J.K. Sundar, S. Gedi, B. Palanivel, S.F. Shaikh, M. Ubaidullah, M.K. Raza, Investigation of heterojunction between α-Fe2O3/V2O5 and g-C3N4 ternary nanocomposites for upgraded photodegradation performance of mixed pollutants: Efficient dual Z-scheme mechanism, J. Alloy. Compd. 902 (2022), 163705, https://doi.org/10.1016/j.jallcom.2022.163705.
[19] S. Zhang, Q. Fan, R. Xia, T.J. Meyer, CO_2 reduction: from homogeneous to heterogeneous electrocatalysis, Acc. Chem. Res. 53 (2020) 255–264, https://doi.org/10.1021/acs.accounts.9b00496.
[20] S.K. Sharma, A. Kumar, G. Sharma, M. Naushad, M. Ubaidullah, A. García-Peñas, Developing a g-C3N4/NiFe2O4 S-scheme hetero-assembly for efficient photocatalytic degradation of cephalexin, Colloids Surf. A: Physicochem. Eng. Asp. 654 (2022), 129968, https://doi.org/10.1016/j.colsurfa.2022.129968.
[21] J. Park, S.S. Lam, Y.-K. Park, B.-J. Kim, K.-H. An, S.-C. Jung, Fabrication of Ni/TiO2 visible light responsive photocatalyst for decomposition of oxytetracycline, Environ. Res. 216 (2023), 114657, https://doi.org/10.1016/j.envres.2022.114657.
[22] R. Xu, H. Huang, W. Wang, L. Ding, Q. Lin, J. Li, Y. Zhang, Y. Han, J. Wang, X. Lu, Direct conversion of water to hydrogen peroxide on single electrode towards partial oxidation of propylene, Chem. Eng. J. 461 (2023), 141748, https://doi.org/10.1016/j.cej.2023.141748.
[23] N.L. Visser, J.C. Verschoor, L.C.J. Smulders, F. Mattarozzi, D.J. Morgan, J. D. Meeldijk, J.E.S. van der Hoeven, J.A. Stewart, B.D. Vandegehuchte, P.E. de Jongh, Influence of carbon support surface modification on the performance of nickel catalysts in carbon dioxide hydrogenation, Catal. Today 418 (2023), 114071, https://doi.org/10.1016/j.cattod.2023.114071.
[24] H. Ju, G. Kaur, A.P. Kulkarni, S. Giddey, Challenges and trends in developing technology for electrochemically reducing CO_2 in solid polymer electrolyte membrane reactors, J. CO_2 Util. 32 (2019) 178–186, https://doi.org/10.1016/j.jcou.2019.04.003.
[25] D.M. Weekes, D.A. Salvatore, A. Reyes, A. Huang, C.P. Berlinguette, Electrolytic CO_2 reduction in a flow cell, Acc. Chem. Res. 51 (2018) 910–918, https://doi.org/10.1021/acs.accounts.8b00010.
[26] K. Ountaksinkul, P. Vas-Umnuay, N. Kasempremchit, P. Bumroongsakulsawat, P. Kim-Lohsoontorn, T. Jiwanuruk, S. Assabumrungrat, Performance comparison of different membrane reactors for combined methanol synthesis and biogas upgrading, Chem. Eng. Process. - Process. Intensif. 136 (2019) 191–200, https://doi.org/10.1016/j.cep.2019.01.009.
[27] J.-B. Vennekoetter, R. Sengpiel, M. Wessling, Beyond the catalyst: How electrode and reactor design determine the product spectrum during electrochemical CO_2 reduction, Chem. Eng. J. 364 (2019) 89–101, https://doi.org/10.1016/j.cej.2019.01.045.

[28] S. Pérez-Rodríguez, F. Barreras, E. Pastor, M.J. Lázaro, Electrochemical reactors for CO_2 reduction: from acid media to gas phase, Int. J. Hydrog. Energy 41 (2016) 19756–19765, https://doi.org/10.1016/j.ijhydene.2016.06.130.
[29] S. Liang, N. Altaf, L. Huang, Y. Gao, Q. Wang, Electrolytic cell design for electrochemical CO_2 reduction, J. CO_2 Util. 35 (2020) 90–105, https://doi.org/10.1016/j.jcou.2019.09.007.
[30] M. Lima, C.M. Godoi, M.C.L. Santos, J. Nandenha, A.O. Neto, R.F.B. De Souza, CO_2 reduction on Cu/C used as a cathode in a polymeric electrolyte reactor - fuel cell type, Int. J. Hydrog. Energy 47 (2022) 4010–4017, https://doi.org/10.1016/j.ijhydene.2021.11.008.
[31] L.M.S. Garcia, N.G.P. Filho, K. Chair, P. Kaur, A.S. Ramos, P.J. Zambiazi, R.F.B. De Souza, L. Otubo, A. Duong, A.O. Neto, Methanol electrosynthesis from CO_2 reduction reaction in polymer electrolyte reactors – fuel cell type using [6,6′-(2,2′-bipyridine-6,6′-diyl)bis(1,3,5-triazine-2,4-diamine)] (dinitrate-O) copper (II) complex, Mater. Today Sustain. 19 (2022), 100177, https://doi.org/10.1016/j.mtsust.2022.100177.
[32] R.F.B. De Souza, É.T. Neto, M.L. Calegaro, E.A. Santos, H.S. Martinho, M.C. dos Santos, Ethanol electro-oxidation on Pt/C Electrocatalysts: an "in situ" Raman spectroelectrochemical study, Electrocatalysis 2 (2011) 28–34, https://doi.org/10.1007/s12678-010-0031-0.
[33] C. Hu, W.-Z. Hung, M.-S. Wang, P.-J. Lu, Phosphorus and sulfur codoped g-C3N4 as an efficient metal-free photocatalyst, Carbon 127 (2018) 374–383, https://doi.org/10.1016/j.carbon.2017.11.019.
[34] M. Deraman, N.E.S. Sazali, M.F.Y.M. Hanappi, N.S.M. Tajuddin, E. Hamdan, M. Suleman, M.A.R. Othman, R. Omar, M.A. Hashim, N.H. Basri, N.S.M. Nor, B.N. M. Dolah, A.M. Noor, M.R.M. Jasni, Graphene/semicrystalline-carbon derived from amylose films for supercapacitor application, J. Phys.: Conf. Ser. 739 (2016), 012085, https://doi.org/10.1088/1742-6596/739/1/012085.
[35] Q. Dong, N. Mohamad Latiff, V. Mazánek, N.F. Rosli, H.L. Chia, Z. Sofer, M. Pumera, Triazine- and heptazine-based carbon nitrides: toxicity, ACS Appl. Nano Mater. 1 (2018) 4442–4449, https://doi.org/10.1021/acsanm.8b00708.
[36] M. Zhou, L. Andrews, Reactions of Laser-Ablated Fe, Co, and Ni with NO: infrared spectra and density functional calculations of MNO+ and M(NO)x (M = Fe, Co, x = 1−3; M = Ni, x = 1, 2), and M(NO)x- (M = Co, Ni; x = 1, 2), J. Phys. Chem. A 104 (2000) 3915–3925, https://doi.org/10.1021/jp993340j.
[37] J.S. Danilova, S.M. Avdoshenko, M.P. Karushev, A.M. Timonov, E. Dmitrieva, Infrared spectroscopic study of nickel complexes with salen-type ligands and their polymers, J. Mol. Struct. 1241 (2021), 130668, https://doi.org/10.1016/j.molstruc.2021.130668.
[38] V. Biju, M. Abdul Khadar, Fourier transform infrared spectroscopy study of nanostructured nickel oxide, Spectrochim. Acta Part A: Mol. Biomol. Spectrosc. 59 (2003) 121–134, https://doi.org/10.1016/S1386-1425(02)00120-8.
[39] K. Maślana, R.J. Kaleńczuk, B. Zielińska, E. Mijowska, Synthesis and characterization of nitrogen-doped carbon nanotubes derived from g-C3N4, Materials (2020) 1349, https://doi.org/10.3390/ma13061349.
[40] R. da Cunha, W.V.F. do Carmo Batista, H.L. de Oliveira, A.C. dos Santos, P.M. dos Reis, K.B. Borges, P.B. Martelli, C.A. Furtado, H. de Fátima Gorgulho, Carbon Xerogel/TiO2 composites as photocatalysts for acetaminophen degradation, J. Photochem. Photobiol. A: Chem. 412 (2021), 113248, https://doi.org/10.1016/j.jphotochem.2021.113248.
[41] L. Jiang, J. Duan, J. Zhu, S. Chen, M. Antonietti, Iron-cluster-directed synthesis of 2D/2D Fe–N–C/MXene superlattice-like heterostructure with enhanced oxygen reduction electrocatalysis, ACS Nano 14 (2020) 2436–2444, https://doi.org/10.1021/acsnano.9b09912.
[42] S. Xie, B. Mei, L. Yu, Z. Nie, M. Li, L. Jiang, J. Duan, Z. Jiang, S. Chen, Size separation of Bi2WO6 nanolayers promoting electroreduction of carbon dioxide to formate, Appl. Surf. Sci. 611 (2023), 155499, https://doi.org/10.1016/j.apsusc.2022.155499.
[43] A. Lewalska-Graczyk, P. Pieta, G. Garbarino, G. Busca, M. Holdynski, G. Kalisz, A. Sroka-Bartnicka, R. Nowakowski, M. Naushad, M.B. Gawande, R. Zbořil, I. S. Pieta, Graphitic carbon nitride–nickel catalyst: from material characterization to efficient ethanol electrooxidation, ACS Sustain. Chem. Eng. 8 (2020) 7244–7255, https://doi.org/10.1021/acssuschemeng.0c02267.
[44] H. Wang, Y. Liu, L. Kong, Z. Xu, X. Shen, S. Premlatha, Porous graphitic carbon nitride nanosheets with three-dimensional interconnected network as electrode for supercapacitors, J. Energy Storage 63 (2023), 106935, https://doi.org/10.1016/j.est.2023.106935.
[45] W.V.F. do Carmo Batista, R. da Cunha, A.C. dos Santos, P.M. dos Reis, C.A. Furtado, M.C. Silva, H. de Fátima Gorgulho, Synthesis of a reusable magnetic photocatalyst based on carbon xerogel/TiO2 composites and its application on acetaminophen degradation, Ceram. Int. 48 (2022) 34395–34404, https://doi.org/10.1016/j.ceramint.2022.08.018.
[46] Y. Li, X. Li, H. Zhang, Q. Xiang, Porous graphitic carbon nitride for solar photocatalytic applications, Nanoscale Horiz. 5 (2020) 765–786, https://doi.org/10.1039/D0NH00046A.
[47] G. Wu, Y. Hu, Y. Liu, J. Zhao, X. Chen, V. Whoehling, C. Plesse, G.T.M. Nguyen, F. Vidal, W. Chen, Graphitic carbon nitride nanosheet electrode-based high-performance ionic actuator, Nat. Commun. 6 (2015), 7258, https://doi.org/10.1038/ncomms8258.
[48] D.F. Wang, Y.Z. Wu, X.H. Yan, J.J. Wang, Q. Wang, C. Zhou, X.X. Yuan, J.M. Pan, X.N. Cheng, Self-assembly synthesis of AgNPs@g-C3N4 composite with enhanced electrochemical properties for supercapacitors, MRS Commun. 9 (2019) 719–725, https://doi.org/10.1557/mrc.2019.25.
[49] J. Liu, H.-T. Kim, S.L. Anderson, Multiphoton ionization and photoelectron spectroscopy of formaldehyde via its 3p Rydberg states, J. Chem. Phys. 114 (2001) 9797–9806, https://doi.org/10.1063/1.1370943.
[50] J. Nandenha, R.M. Piasentin, L.M.G. Silva, E.H. Fontes, A.O. Neto, R.F.B. de Souza, Partial oxidation of methane and generation of electricity using a PEMFC, Ionics 25 (2019) 5077–5082, https://doi.org/10.1007/s11581-019-03186-z.
[51] M.C.L. Santos, L.C. Nunes, L.M.G. Silva, A.S. Ramos, F.C. Fonseca, R.F.B. de Souza, A.O. Neto, Direct alkaline anion exchange membrane fuel cell to converting methane into methanol, ChemistrySelect 4 (2019) 11430–11434, https://doi.org/10.1002/slct.201902421.